INTERNATIONAL JOURNAL FOR NUMERICAL METHODS IN FLUIDS
Int. J. Numer. Meth. Fluids 2006; **51**:1379–1405
Published online 4 January 2006 in Wiley InterScience (www.interscience.wiley.com). DOI: 10.1002/fld.1169

Prediction of developing turbulent flow in 90°-curved ducts using linear and non-linear low-Re k–ε models

M. Raisee[1,*,†], H. Alemi[1,‡] and H. Iacovides[2,§]

[1]*Department of Mechanical Engineering, Faculty of Engineering, University of Tehran, Tehran, Iran*
[2]*School of Mechanical, Aerospace and Civil Engineering, University of Manchester, Manchester, U.K.*

SUMMARY

This paper reports the outcome of applying two different low-Reynolds-number eddy-viscosity models to resolve the complex three-dimensional motion that arises in turbulent flows in ducts with 90° bends. For the modelling of turbulence, the Launder and Sharma low-Re k–ε model and a recently produced variant of the cubic non-linear low-Re k–ε model have been employed. In this paper, developing turbulent flow through two different 90° bends is examined: a square bend, and a rectangular bend with an aspect ratio of 6. The numerical results indicate that for the bend of square cross-section the curvature induces a strong secondary flow, while for the rectangular cross-section the secondary motion is confined to the corner regions. For both curved ducts, the secondary motion persists downstream of the bend and eventually slowly disappears. For the bend of square cross-section, comparisons indicate that both turbulence models can produce reasonable predictions. For the bend of rectangular cross-section, for which a wider range of data is available, while both turbulence models produce satisfactory predictions of the mean flow field, the non-linear k–ε model returns superior predictions of the turbulence field and also of the pressure and friction coefficients. Copyright © 2006 John Wiley & Sons, Ltd.

KEY WORDS: turbulent flow; curved ducts; turbulence modelling

1. INTRODUCTION

Developing turbulent flow through 90°-curved ducts occurs in several engineering applications such as the draft tube of hydraulic turbines and centrifugal pumps. Moreover, there are generic similarities with flows in turbine cascade passages. Consequently, detailed information about flow in 90°-curved ducts (e.g. 90° bends) can be very valuable for the optimum design of engineering devices. The assessment of how effective current CFD practices are in predicting such flows is, therefore, of strong practical relevance.

*Correspondence to: M. Raisee, Department of Mechanical Engineering, Faculty of Engineering, University of Tehran, Tehran, Iran.
†E-mail: mraisee@ut.ac.ir
‡E-mail: h_alemi@me.ut.ac.ir
§E-mail: h.iacovides@manchester.ac.uk

Received 23 December 2004
Revised 18 November 2005
Accepted 22 November 2005

In two-dimensional flows through curved channels, the most critical problem is the modelling of effects of streamline curvature on the turbulence field. The effects of the streamline curvature on turbulence are caused by the centrifugal force. They are represented in the turbulence kinetic energy, stress transport and scale equations by terms involving interaction of different stress and rate of strain components. Early attempts in predicting the behaviour of such flows showed that conventional effective viscosity models (EVM) have all failed to reproduce these curvature effects. As shown by Iacovides and Li [1], to reproduce the measured mean flow development the use of second-moment closures becomes necessary. In three-dimensional flows through curved ducts of moderate curvature, the main flow feature is the curvature-induced secondary motion. This is driven by the imbalance between the radial (cross-duct) pressure gradient and the centrifugal force. At the near-wall regions, due to the low axial velocity the centrifugal force is weak and the radial pressure gradient force drives the fluid towards the inner side of the curved duct. In the duct core, where the axial velocity is high, the centrifugal force is the dominant one and drives the fluid towards the outer side of the curved duct. This secondary motion causes a highly three-dimensional flow field in curved ducts, with the faster fluid accumulating along the outer side and the slower displaced along the inner wall. The enhanced mixing also increases pressure losses and, in the case of heated ducts, overall wall heat transfer. The curvature-induced secondary motion can thus be reproduced even in computations using EVMs.

As the secondary motion is strongest within the near-wall regions, where the imbalance between the centrifugal and radial pressure forces is greatest, one would expect that only turbulence models that resolve the near-wall motion would be able to reproduce this flow feature correctly. This has been shown to be the case by the work of Choi *et al.* [2], who instead of using the high-Re turbulence models with the wall-function approximation, adopted a two-layer approach. This allows the mean flow equations to be integrated up to the wall, using simple models of near-wall turbulence. Choi *et al.* [2] also showed that replacement of high-Re k–ε in the duct core with an algebraic second-moment closure resulted in further improvements in the predicted flow field. This suggests that the effects of turbulence anisotropy, while less critical than in two-dimensional flows through curved passages, are certainly not negligible.

Turbulent flow through 90°-curved ducts has been extensively studied by many research groups, using experimental techniques, in order to provide information about flow behaviour. Measurements on turbulent flow in circular curved ducts were reported by Enayet *et al.* [3], Anwer *et al.* [4] and Sudo *et al.* [5]. These experiments help researchers develop an understanding of the development of turbulent flow in curved ducts. In the following, attention is mainly focused on more related published works on turbulent flow through 90°-curved ducts of either rectangular or square cross-section. Due to the large number of such studies available in the literature, only some of the published works in this area are summarized. Humphrey and Whitelaw [6] reported measurements for turbulent flow through a 90° bend of square cross-section and strong curvature and found that the pressure-driven secondary flows were much stronger than the stress-driven secondary flows. Taylor *et al.* [7], using LDA, measured velocity components and wall-pressure of developing turbulent flow through a square 90° bend with a short upstream tangent. They found that the boundary layer thickness at the start of the bend is important to the flow development within the bend. It was also noted that turbulent flow in an identical duct of mild curvature results in a weaker secondary motion. Kim and Patel [8], using a five-hole pressure probe

and two-sensor hot-wire probes measured mean velocities and Reynolds stresses for developing turbulent flow in a 90°-curved duct of rectangular cross-section. Their data showed that within the bend there is an extensive region of two-dimensional boundary layers under strong stream-wise curvatures and attendant pressure gradients. Moreover, their results showed the development of the pressure-driven secondary motion in the corner region which eventually leads to the formation of a longitudinal vortex on the convex wall. Sudo *et al.* [9], using the method of an inclined hot-wire obtained mean velocity and Reynolds stress measurements for turbulent airflow through a square-sectioned 90°-curved duct. They presented the details of both main stream and secondary flow in the cross-section and concluded that the development of main stream is related to the secondary flow induced in the cross-section, pressure gradients near the inner and outer walls, and the centrifugal force. Mokhtarzadeh-Dehghan and Yuan [10], using hot-wire anemometry have recently measured the details of developing turbulent flow in a 90° square duct and provided quantitative data for the bursting period of turbulent boundary layers subjected to convex and concave curvatures of the bend.

On the whole, it can be concluded that developing turbulent flow in 90° bends is a very complex flow which is influenced by various parameters such as the duct aspect ratio, the boundary layer thickness at the start of curvature and also the ratio between the radius of curvature and the hydraulic radius of the duct. Due to these complexities, the experimental data may be used in CFD code validation to examine not only the capabilities of numerical schemes, but also to investigate the performance of the turbulence models. In the literature, there are a few papers that reported numerical results for turbulent flow through 90° square ducts. One of the earliest numerical attempts to simulate turbulent flow through 90° bends was reported by Kreskovsky *et al.* [11]. They employed a simple closure model for the Reynolds stresses to predict the 90° bend flow of Taylor *et al.* The level of agreement achieved was reasonably good, though there was insufficient growth of the boundary layer on the convex inner surface toward the end of the bend where the flow on that surface encountered a substantial adverse pressure gradient. In a later study, Iacovides *et al.* [12], using a two-layer EVM, performed numerical computations for Taylor's experiment. The standard k–ε eddy-viscosity was employed for the main flow region, while the mixing-length hypothesis was used across the low-Re near-wall region. The computational results showed that the curvature induces a pair of counter-rotating vortices within the duct cross-section. The level of agreement was better than obtained by Kreskovsky *et al.* using a simple mean-field closure.

In this paper, a numerical investigation has been undertaken to study developing turbulent flow through two different 90°-curved ducts: a square duct and a rectangular duct. In contrast to the mixing-length and zonal models used in earlier investigations, here the low-Re models of turbulence are employed. The main objectives of the present contribution are to examine how curvature alters flow development in the curved ducts and to explore the predictive capabilities of a recently modified variant of the cubic non-linear k–ε model, relative to those of the linear low-Re k–ε model, in predicting flow characteristics in curved ducts. The version of the cubic non-linear k–ε model has been recently applied for the computations of convective heat transfer in impinging and separating flows by Craft *et al.* [13] and in ribbed cooling passages by Raisee *et al.* [14] with encouraging success. The present study attempts to further examine the capabilities of the non-linear k–ε model in predicting flow characteristics in curved passages.

2. GEOMETRY INVESTIGATED

Figure 1(a) shows the geometry of the first test case investigated in the present study. The bend is of square cross-section and has a bend radius to duct height ratio (R_c/H) of 2.3. The lengths of the duct before and after the curved section are $9H$ and $26H$, respectively. The upstream length of the computational domain is set to $9H$, because when starting with uniform inlet conditions, the resulting predictions best matched the available data at the first measured location just before the bend. The downstream length is selected as $26H$, based on the empirical correlation for entrance-length given by Munson *et al.* [15]. The available experimental data for this geometry are stream-wise and cross-stream velocity components and the pressure coefficient distribution. The experimental data were collected by Taylor *et al.* [7] at a Reynolds number, based on the hydraulic diameter ($D_h = H$) and the bulk velocity (U_b), of 40 000 using LDA. Measured stream-wise and cross-stream velocities at selected locations as well as the pressure coefficient distributions along the curved section of

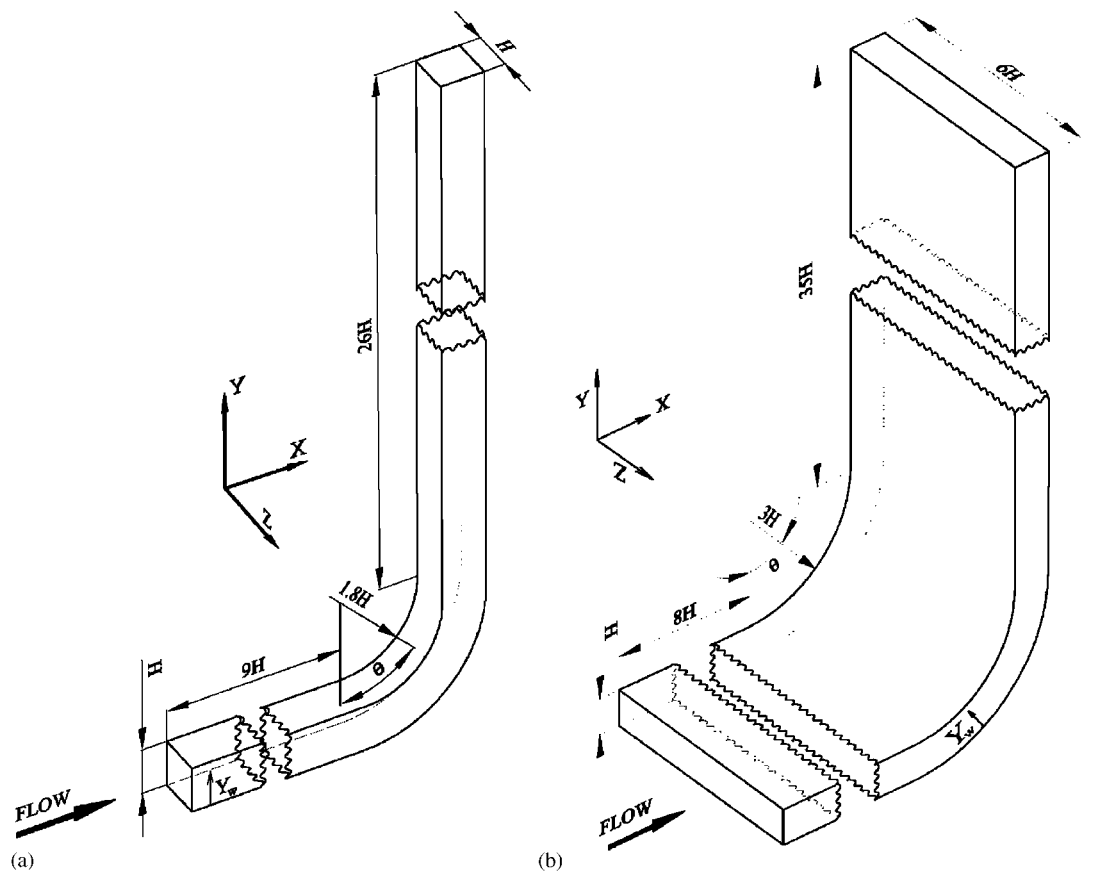

Figure 1. The geometry of 90° bends examined: (a) square 90°-curved duct; and (b) rectangular 90°-curved duct.

the duct, are used for comparisons. Figure 1(b) shows the geometry of the second test case examined in this paper. The bend is of rectangular cross-section with an aspect ratio (W/H) of 6 and the lengths of the duct before and after the curved section are $8H$ and $35H$, respectively. The reason of selecting these lengths is similar to that mentioned above for the curved duct of square cross-section. For this configuration, flow measurements have been made by Kim and Patel [8] at a Reynolds number, based on the centreline velocity (U_c) and the duct's height (H), of 224 000. For this case, experimental data include velocity and Reynolds stress profiles, pressure coefficient and friction factor distribution.

3. GOVERNING EQUATIONS

All the flow equations are presented in Cartesian tensor notation.

3.1. Mean flow equations

For a steady incompressible flow, the conservation laws of mass and momentum are written as

Continuity:

$$\frac{\partial U_j}{\partial x_j} = 0 \tag{1}$$

Momentum:

$$\frac{\partial (U_j U_i)}{\partial x_j} = -\frac{1}{\rho}\frac{\partial P}{\partial x_i} + \frac{\partial}{\partial x_j}\left(\nu \frac{\partial U_i}{\partial x_j} - \overline{u_i u_j}\right) \tag{2}$$

where P is the pressure, upper and lower case U's denote mean and fluctuating velocities, and $\overline{u_i u_j}$ is the unknown Reynolds stress.

3.2. Turbulence modelling equations

The turbulence models employed for computation are the Launder and Sharma [16] low-Re k–ε model, and a recently developed version of non-linear low-Re k–ε model [13]. Computations with both models have been carried out with inclusion of the new differential form of length-scale correction term 'NYP' [17] which is free from any explicit wall distance, in the dissipation rate equation.

3.2.1. Linear low-Re k–ε model. In this turbulence model, the Reynolds stress tensor is obtained from the eddy-viscosity approximation:

$$\overline{u_i u_j} = \frac{2}{3}\delta_{ij} k - \nu_t \left(\frac{\partial U_i}{\partial x_j} + \frac{\partial U_j}{\partial x_i}\right) \tag{3}$$

and the turbulent viscosity, ν_t, is obtained from:

$$\nu_t = c_\mu f_\mu \frac{k^2}{\tilde{\varepsilon}} \tag{4}$$

Table I. Empirical constants for the k–ε model.

c_μ	$c_{\varepsilon 1}$	$c_{\varepsilon 2}$	σ_k	σ_ε
0.09	1.44	1.92	1.0	1.22

To obtain ν_t, transport equations for the turbulence kinetic energy, k, and homogeneous dissipation rate, $\tilde{\varepsilon}$, are solved. The transport equation for the turbulent kinetic energy is written as

$$\frac{\partial}{\partial x_j}(U_j k) = \frac{\partial}{\partial x_j}\left[\left(\nu + \frac{\nu_t}{\sigma_k}\right)\frac{\partial k}{\partial x_j}\right] + P_k - \tilde{\varepsilon} - 2\nu\left(\frac{\partial\sqrt{k}}{\partial x_j}\right)^2 \tag{5}$$

The dissipation rate of the turbulent kinetic energy is obtained by solving the equation:

$$\frac{\partial}{\partial x_j}(U_j\tilde{\varepsilon}) = \frac{\partial}{\partial x_j}\left[\left(\nu + \frac{\nu_t}{\sigma_\varepsilon}\right)\frac{\partial\tilde{\varepsilon}}{\partial x_j}\right] + f_1 c_{\varepsilon 1}\frac{\tilde{\varepsilon}}{k}P_k - f_2 c_{\varepsilon 2}\frac{\tilde{\varepsilon}^2}{k} + E + S_\varepsilon \tag{6}$$

where the variable $\tilde{\varepsilon}$ is the homogeneous dissipation rate which can be related to the real dissipation rate through:

$$\tilde{\varepsilon} = \varepsilon - 2\nu\left(\frac{\partial\sqrt{k}}{\partial x_j}\right)^2 \tag{7}$$

The damping functions f_μ, f_1 and f_2 are given by

$$f_\mu = \exp[-3.4/(1 + 0.02\tilde{R}_t)^2], \quad f_1 = 1, \quad f_2 = 1 - 0.3\exp(-\tilde{R}_t^2) \tag{8}$$

where $\tilde{R}_t = k^2/\nu\tilde{\varepsilon}$ is the local turbulent Reynolds number.

The model constants are given in Table I.

The term E was first introduced by Jones and Launder [18] and is expressed as

$$E = 2\nu\nu_t\left(\frac{\partial^2 U_i}{\partial x_j \partial x_k}\right)^2 \tag{9}$$

The extra source term, S_ε, stands for the 'NYP' correction term which was first proposed by Iacovides and Raisee [17] and is written as

$$S_\varepsilon = \mathrm{NYP} = \max\left[C_\omega F(F+1)\frac{\tilde{\varepsilon}^2}{k},\ 0\right] \tag{10}$$

where

$$F = \{[(\partial l/\partial x_j)(\partial l/\partial x_j)]^{1/2} - \mathrm{d}l_e/\mathrm{d}y\}/C_l \tag{11}$$

represents the difference between the predicted length-scale gradient, with $l = k^{3/2}/\tilde{\varepsilon}$, and the 'equilibrium length-scale gradient', $\mathrm{d}l_e/\mathrm{d}y$, defined by

$$\mathrm{d}l_e/\mathrm{d}y = C_l[1 - \exp(-B_\varepsilon R_t)] + B_\varepsilon C_l R_t \exp(-B_\varepsilon R_t) \tag{12}$$

where $C_l = 2.55$, $B_\varepsilon = 0.1069$ and $C_\omega = 0.83$.

3.2.2. Non-linear low-Re k–ε model. It is well known that linear eddy-viscosity models such as the k–ε model exhibit numerous weaknesses, including an inability to capture normal stress anisotropy and insensitivity to stream-line curvature. Second-moment closure models, on the other hand, account for several of the key features of turbulence that are misrepresented by linear eddy-viscosity models. However, these models are considerably more complex and require higher CPU time than eddy-viscosity model. Gatski and Speziale [19] proposed non-linear models which are basically explicit algebraic stress models derived from second moment closures. Although such models ensure that they return the same results as the underlying stress-transport scheme under equilibrium conditions, their performance in complex, highly non-equilibrium flows has not been widely tested.

A simpler alternative for approximating of the Reynolds stresses is to extend the strain–stress relation of the linear eddy-viscosity model, by adding all the higher order (second or second and third order) non-linear combinations of the strain and vorticity rate tensors that satisfy the kinematic constraints of the turbulent stress tensor. The coefficient of these terms are then determined with reference to a range of basic flows. These non-linear strain–stress relations have the ability to produce the differences between the normal stresses and thus can extend the model's applicability, by allowing it to predict flows in which the anisotropy of turbulence is important, such as flows involving turbulence-driven secondary motions. The majority of earlier works in this direction (e.g. References [20, 21]) only retained terms up to quadratic order in the mean velocity gradients. However, it was found that improvements in predictions were only achieved for limited types of flow for any one particular model. This led Suga [22] to develop a non-linear eddy viscosity model (NLEVM) with terms up to cubic order, in order exhibit correct sensitivity to streamline curvature. In this turbulence model, the turbulent stresses are obtained via the constitutive relation:

$$
\begin{aligned}
a_{ij} = \frac{\overline{u_i u_j}}{k} - \frac{2}{3}\delta_{ij} = & -\frac{\nu_t}{k} S_{ij} + c_1 \frac{\nu_t}{\tilde{\varepsilon}} \left(S_{ik}S_{kj} - \frac{1}{3} S_{kl}S_{kl}\delta_{ij} \right) \\
& + c_2 \frac{\nu_t}{\tilde{\varepsilon}} (\Omega_{ik}S_{kj} + \Omega_{jk}S_{ki}) + c_3 \frac{\nu_t}{\tilde{\varepsilon}} \left(\Omega_{ik}\Omega_{jk} - \frac{1}{3}\Omega_{lk}\Omega_{lk}\delta_{ij} \right) \\
& + c_4 \frac{\nu_t k}{\tilde{\varepsilon}^2} (S_{ki}\Omega_{lj} + S_{kj}\Omega_{li}) S_{kl} \\
& + c_5 \frac{\nu_t k}{\tilde{\varepsilon}^2} \left(\Omega_{il}\Omega_{lm}S_{mj} + S_{il}\Omega_{lm}\Omega_{mj} - \frac{2}{3} S_{lm}\Omega_{mn}\Omega_{nl}\delta_{ij} \right) \\
& + c_6 \frac{\nu_t k}{\tilde{\varepsilon}^2} S_{ij}S_{kl}S_{kl} + c_7 \frac{\nu_t k}{\tilde{\varepsilon}^2} S_{ij}\Omega_{kl}\Omega_{kl}
\end{aligned} \tag{13}
$$

where S_{ij} and Ω_{ij} are strain and vorticity rate tensors, respectively,

$$
S_{ij} = \left(\frac{\partial U_i}{\partial x_j} + \frac{\partial U_j}{\partial x_i} \right), \quad \Omega_{ij} = \left(\frac{\partial U_i}{\partial x_j} - \frac{\partial U_j}{\partial x_i} \right) \tag{14}
$$

Table II. Values of coefficients in the non-linear k–ε model.

c_1	c_2	c_3	c_4	c_5	c_6	c_7
-0.1	0.1	0.26	$-10c_\mu^2$	0	$-5c_\mu^2$	$5c_\mu^2$

The model coefficients, c_1–c_7, have been calibrated by Craft *et al.* [23], by reference to several flows, including homogeneous shear flows, swirling flows and curved channel flows. The values of these coefficients are given in Table II.

The k and $\tilde{\varepsilon}$ transport equations and eddy-viscosity formulation are similar to those of linear model, however, for modelling of c_μ the following expression was proposed by Craft *et al.* [13]:

$$c_\mu = \min\left[0.09,\ \frac{12}{1+3.5\eta+f_{RS}}\right] \tag{15}$$

with

$$\eta = \max(\tilde{S}, \tilde{\Omega}) \tag{16}$$

where strain and vorticity invariants are expressed as

$$\tilde{S} = \frac{k}{\tilde{\varepsilon}}\sqrt{0.5S_{ij}S_{ij}}, \quad \tilde{\Omega} = \frac{k}{\tilde{\varepsilon}}\sqrt{0.5\Omega_{ij}\Omega_{ij}} \tag{17}$$

and

$$f_{RS} = 0.235[\max(0,\ \eta - 3.333)]^2 \exp(-\tilde{R}_t/400) \tag{18}$$

The viscous damping of ν_t is provided by the function f_μ:

$$f_\mu = 1 - \exp\left\{-\left(\frac{\tilde{R}_t}{90}\right)^{1/2} - \left(\frac{\tilde{R}_t}{400}\right)^2\right\} \tag{19}$$

The near-wall source term E is now expressed as

$$E = \begin{cases} 0.0022\dfrac{\tilde{S}\nu_t k^2}{\tilde{\varepsilon}}\left(\dfrac{\partial^2 U_i}{\partial x_k \partial x_i}\right)^2 & \text{for } \tilde{R}_t \leqslant 250 \\ 0 & \text{for } \tilde{R}_t > 250 \end{cases} \tag{20}$$

In this model, the length scale correction term is still required in the dissipation rate equation to correct for over-predicted length scales in boundary layers subjected to adverse pressure gradients and in separated flows. However, in order to reduce the amount of correction in the

regions of high η, Craft *et al.* [13] proposed that the coefficient C_ω is taken as

$$C_\omega = \frac{0.83 \min(1, \tilde{R}_t/5)}{0.8 + 0.7(\eta'/3.33)^{1/2} \exp(-\tilde{R}_t/125)} \tag{21}$$

where

$$\eta' = \max\left[\frac{k}{\tilde{\varepsilon}}, \sqrt{\frac{\nu}{\varepsilon}}\right]\eta \tag{22}$$

The limited $\tilde{R}_t$-dependent damping is included for numerical stability.

4. NUMERICAL ASPECTS

The calculations presented here have been obtained using the modified version of the STREAM code, an open source research code, developed at UMIST by Lien and Leschziner [24]. This 'in-house' research code of the UMIST group, employs a finite-volume strategy in which a non-orthogonal and body-fitted grid system is used and all transported properties are stored in a fully collocated manner. Advective volume-face fluxes are approximated using a bounded version of the upstream quadratic interpolation scheme, QUICK, described in Reference [25]. To evaluate the pressure field the well-known SIMPLE pressures correction algorithm has been used. To avoid stability problems associated with pressure–velocity decoupling, the Rhie and Chow [26] interpolation scheme is also employed. The STREAM code has been successfully used by many researchers for computation of various complex flows. Examples of such works are References [24, 27–29].

The flow through 90°-curved ducts considered in this investigation is governed by elliptic partial differential equations, and these require the prescription of boundary conditions along the entire perimeter of the solution domain. Since the inlet boundary conditions are not available form the experimental data, a uniform flow inlet condition is imposed at the duct entry by setting the U-velocity equal to the bulk velocity and V and W velocities to zero. The value of turbulent kinetic energy (k) at the inlet is set to $(0.03U_b)^2$. The value of ε is subsequently computed from $k^{3/2}/l$ with $l = 0.1H$. It should be mentioned that several computations have been performed to examine the influence of k and ε levels at the inlet on the flow predictions. The results of these investigations showed that flow field predictions vary little with these changes. The values of normal stresses subsequently set to $2/3k$, while the shear stresses are set to zero. These uniform flow inlet conditions were imposed at $8H$ and $9H$ upstream of the bend entry for the square and rectangular ducts, respectively. As mentioned in Section 2, these upstream lengths of the computational domains were selected, because when starting with uniform inlet conditions, the resulting predictions best matched the available data at the first measured location just before the bend. At the downstream boundary, zero gradient conditions were imposed for all variables except pressure. A uniform pressure difference is imposed across the exit plane, determined from overall continuity considerations.

As shown in Figure 2(a), due to symmetry of the curved square duct, only half of the cross-section is resolved using a body-fitted mesh. In this figure, the origin of the coordinate system corresponds on the centre of curvature. The mesh consists of $70 \times 71 \times 35$ nodes in stream-wise, cross-stream, and span-wise directions, respectively. In the stream-wise direction,

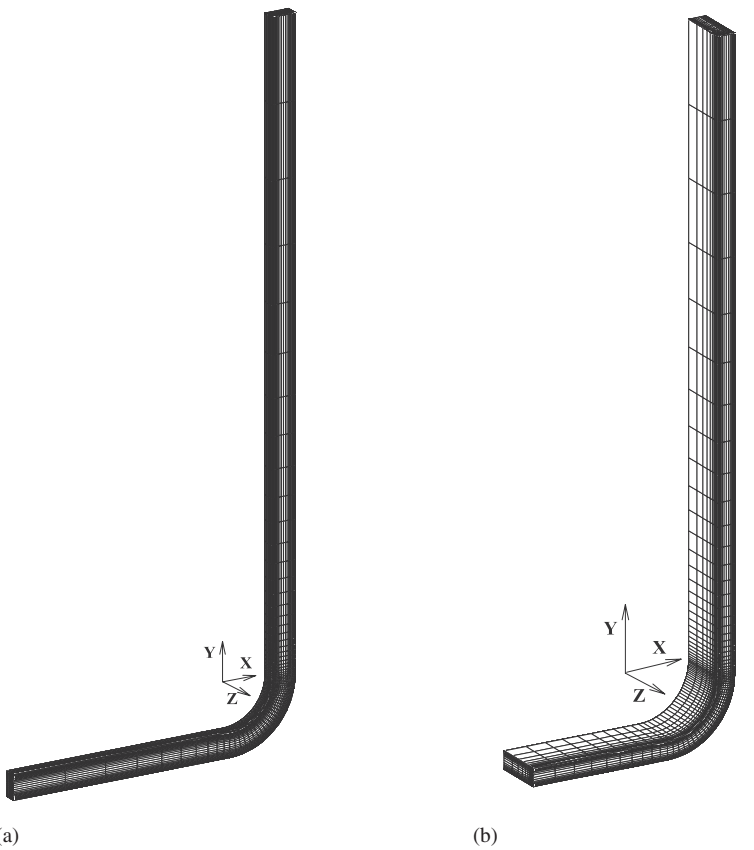

Figure 2. Computational grids with $70 \times 71 \times 35$ nodes in stream-wise, cross-stream, and span-wise directions.

15 nodes are located along the upstream-length, 35 nodes cover the curved section and 20 nodes are placed along the downstream-length of the duct.

A similar mesh with the same number of grid nodes was also used for the computations in the curved duct of rectangular cross-section, see Figure 2(b). Although the aspect ratio of the rectangular duct is much higher than that of a square duct, experimental data of Kim and Patel [8] indicates a wide region of two-dimensional flow along the span-wise (z) direction. This justifies the number of grid points used in z direction for the curved duct of rectangular cross-section. The y^+ value of the near-wall nodes was kept, in all computations, to levels of less than unity. To assess the accuracy of the results, a series of grid independency tests have been carried out using a medium ($50 \times 51 \times 25$) and the fine ($70 \times 71 \times 35$) mesh. For both geometries, the predicted velocity profiles at two stream-wise locations, one upstream of the curved section and one within the bend, are shown in Figures 3 and 4. It can be seen that the predicted stream-wise velocity profiles on the $70 \times 71 \times 35$ mesh are practically identical to those obtained on the $50 \times 51 \times 25$ mesh. This indicates that for both geometries investigated, results obtained on the $70 \times 71 \times 35$ mesh can be regarded as grid-independent.

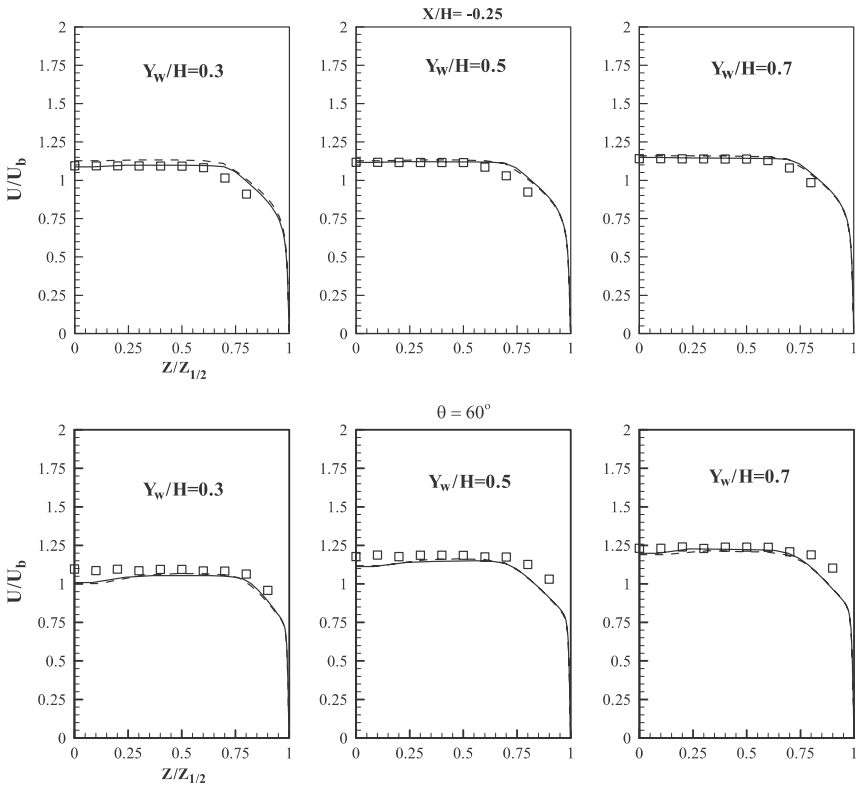

Figure 3. Predicted stream-wise velocity component for flow through square 90° bend using linear k–ε model. Open squares: data [7]; dashed curve: medium ($50 \times 51 \times 25$) grid; solid curve: fine ($70 \times 71 \times 35$) grid.

5. RESULTS AND DISCUSSION

5.1. Curved duct of square cross-section

The computed velocity vectors, obtained with the non-linear k–ε model, at the vertical mid-plane of the duct are shown in Figure 5. An enlargement of the bend region is also included, to highlight the more interesting features of the flow development. The linear low-Re k–ε model velocity vectors were similar and thus are not shown here. As can be observed, fluid enters uniformly and as a result of flow development the boundary layer thickness grows along the straight duct. Within the bend, the fluid accelerates along the convex (suction) surface up to $\theta = 45°$ and then starts to decelerate. It is observed that the opposite occurs along the concave (pressure) surface. The initial flow acceleration and deceleration along the convex and concave surfaces of the bend, respectively, stem from the pressure gradients that develop at the bend entry. Due to the action of the centrifugal force, along the convex (inner) side the pressure drops at the bend entry, while along the concave (outer) side the pressure rises. Consequently, a favourable pressure gradient is generated along the inner side and an adverse one along the outer side, at the bend entry. The convective effects of the secondary motion that

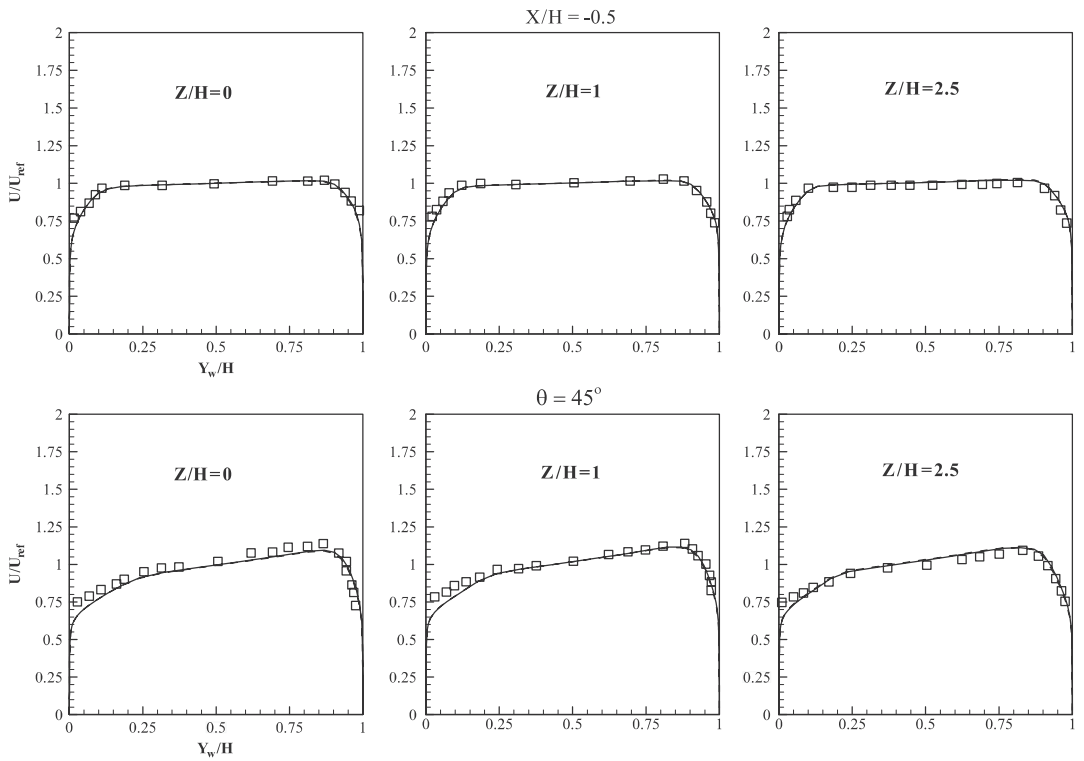

Figure 4. Predicted stream-wise velocity component for flow through rectangular 90° bend using linear k–ε model. Open squares: data [8]; dashed curve: medium ($50\times51\times25$) grid; solid curve: fine ($70 \times 71 \times 35$) grid.

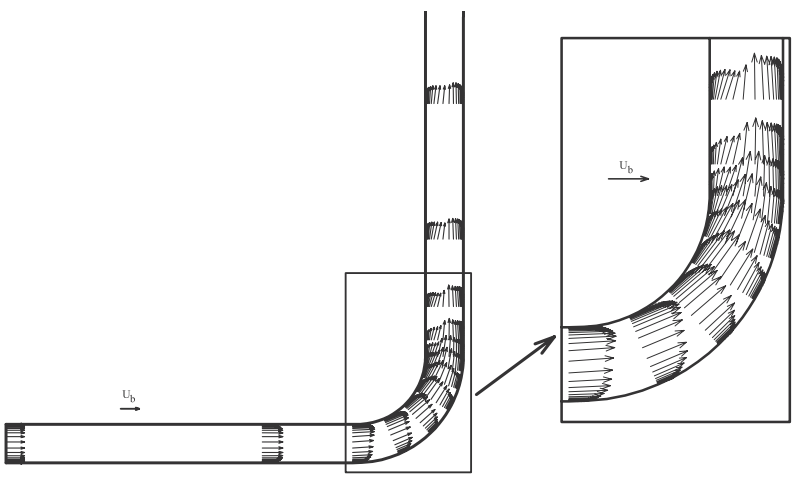

Figure 5. Predicted flow field in middle plane of the square 90° bend using the non-linear k–ε model.

develops within the bend and also the stream-wise pressure gradients at the bend exit, which have the opposite sign to those at the entry, account for the subsequent deceleration along the convex surface and the corresponding acceleration along the concave surface. After the curved section of the duct, fluid velocity gradually decreases along the outer surface and increases along the inner surface of the straight duct, until it reaches to the fully developed condition. It is also worth noting that towards the bend exit, a strong span-wise gradient in the mean velocity develops in the duct core. This suggests strong three-dimensionalities in the flow.

Figure 6 shows the predicted stream-wise velocity contours (U/U_b) and secondary flow vectors, at three cross-sectional planes, using the linear and non-linear k–ε models. It can be seen that just before the bend entry, at $X/H = -0.25$, due to the effects of the entry-plane streamwise pressure gradients, the core fluid is displaced towards the convex surface. Within the bend, the duct curvature induces two pairs of counter-rotating secondary vortices across the duct, as seen at $\theta = 60°$ and $Y/H = 0.25$. The pair of larger vortices is the classical curvature induced secondary flow pattern, which transfers fluid from the concave surface to the convex surface along the side walls and then returns it to the concave surface through the centre of the duct. The pair of smaller counter-rotating vortices is close to the concave surface, and their presence, which has been reported in earlier studies of curved duct flows, such as Reference [2], is due to the instability of the boundary layer along the concave wall. It is evident from the shape of the streamwise velocity contours, that the secondary motion significantly alters the distribution of stream-wise velocity across the duct. The smaller vortices bring the low momentum fluid from the side walls to the symmetry plane in the vicinity of the concave surface. This accounts for the strong span-wise gradient in mean velocity observed in Figure 5. It can be seen that the differences between the two sets of computations are insignificant. Both turbulence models produce more or less similar stream-wise velocity contours and secondary velocity cells.

A major, but interesting, difference between the present results with those reported by Iacovides *et al.* [12] for an identical geometry is that in the earlier study only one pair of counter-rotating secondary motions was predicted across the duct cross-section using a zonal k–ε model, while the present models produce two. There are two possible reasons for these predictive differences. First, the use of the zonal model, by Iacovides *et al.* [12], with a fixed turbulent length-scale across the near-wall regions may be inappropriate in regions of strong stream-wise pressure gradient, such as the bend entry and exit regions. Second, the Iacovides *et al.* [12] study employed a semi-elliptic flow solver, which involved a marching solution for all flow variables except for pressure and also the use of upwind differencing in the stream-wise direction. In contrast to that earlier study, here the calculation are fully elliptic and the QUICK scheme, all be in a bounded form, is used in all directions and for all variables. One would thus expect the present computations of the secondary flow to be more realistic.

Comparisons between the computed and measured stream-wise velocity component across three stream-wise planes are presented in Figure 7. Upstream of the bend at $X/H = -0.25$, it is seen that the flow is still developing and, consistent with secondary flow shown in Figure 6, the core fluid is somewhat displaced towards the convex surface. At this location, both turbulence models return similar profiles which are also close to the experimental data. Within the curved duct at $\theta = 60°$, both models correctly predict the stream-wise velocity in the core region, though close to the side wall the non-linear k–ε model performs slightly better. Downstream of the curved section at $Y/H = 0.25$, it is seen that, due to the secondary flow, low-momentum fluid is accumulated near the convex surface ($Y_w/H = 0.7$). At this

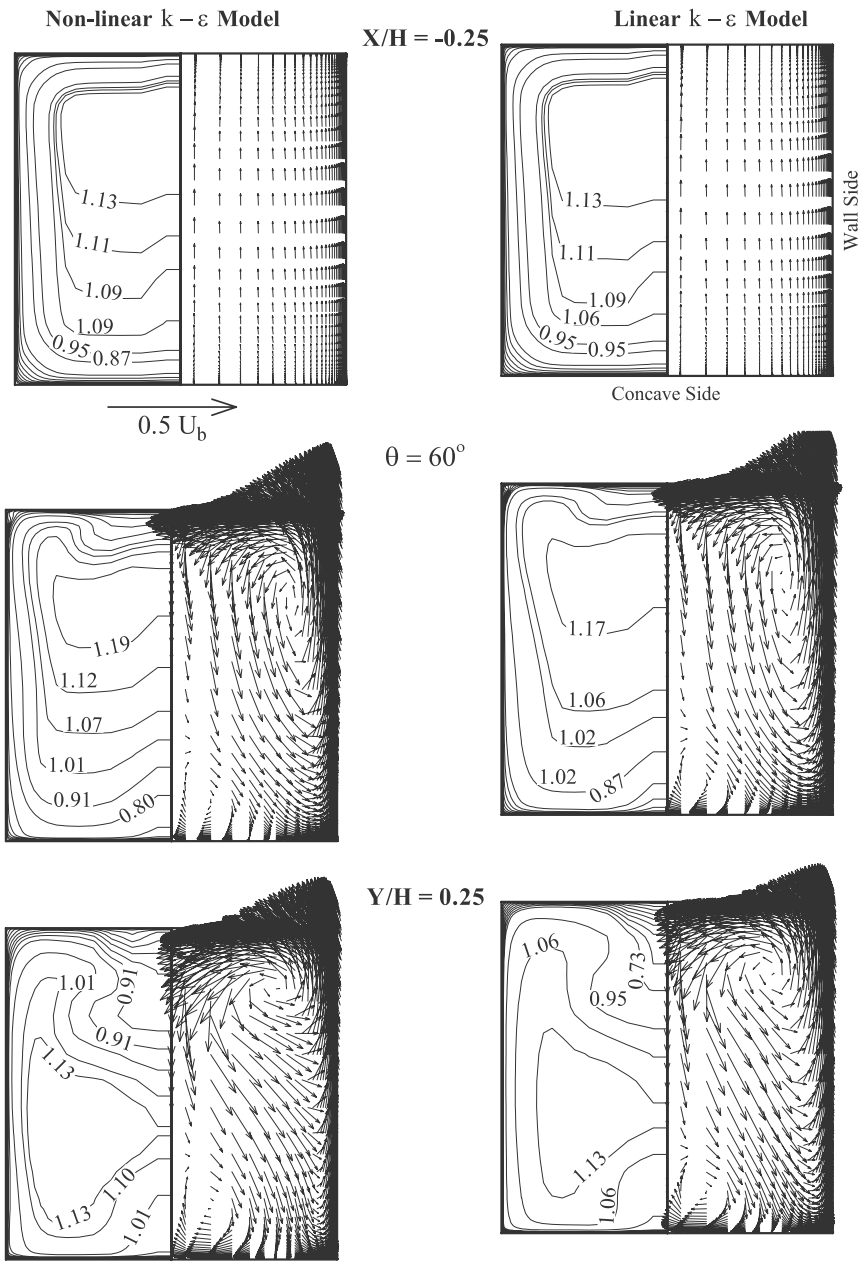

Figure 6. The predicted stream-wise velocity contours and secondary flow vectors using the linear and non-linear k–ε models.

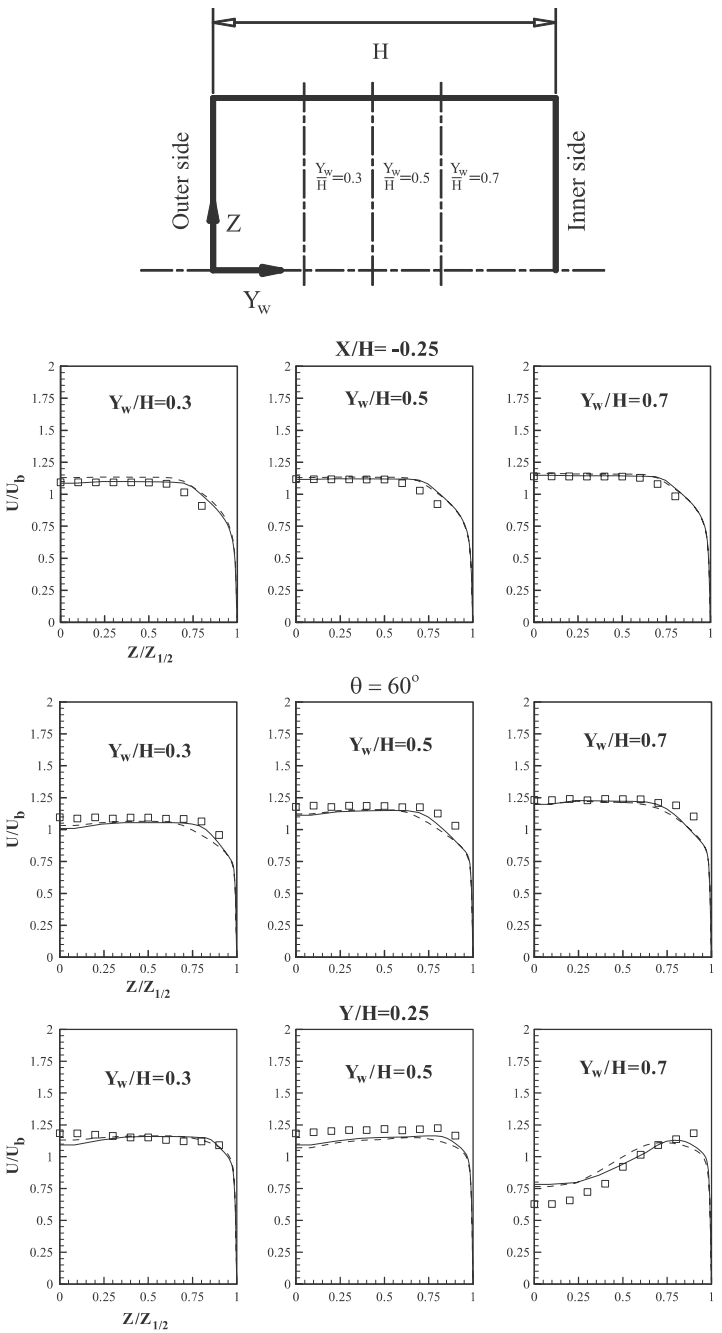

Figure 7. Comparisons between predicted and measured stream-wise velocity component for flow through square 90° bend. Open squares: data [7]; dashed curve: linear k–ε model; solid curve: non-linear k–ε model.

location ($Y/H = 0.25$), both the linear and non-linear models return the correct behaviour close to the concave wall ($Y_w/H = 0.3$), but some discrepancies are observed between predictions and measurements along the symmetry line close to the convex surface ($Y_w/H = 0.7$) and the plane halfway between the concave and convex walls ($Y_w/H = 0.5$). Both turbulence models under-predict the measured values of the stream-wise velocity at $Y_w/H = 0.5$. At $Y_w/H = 0.7$ the stream-wise velocity is under-predicted near the side wall, while it is over-predicted in the core of the duct. This suggests that the strength of the secondary motion is under-predicted.

The corresponding comparisons for the cross-stream velocity component are presented in Figure 8. Upstream of the curved section at $X/H = -0.25$, the experiments show that the cross-stream velocity is small but directed towards the convex surface, a feature consistent with the secondary flow at $X/H = -0.25$ shown in Figure 6, and the presence of a cross-stream pressure gradient upstream of the bend. It is observed that both turbulence models correctly return a small uniform and positive cross-stream velocity. Within the bend at $\theta = 60°$, the measurements reveal that the fluid near the symmetry plane moves away from the convex surface while the fluid near the side wall moves towards it, forming in a large pressure-driven secondary flow which is already shown in Figure 6. It is observed that both turbulence models correctly reproduce the variation as well as the levels of the cross-stream velocity at this location. Downstream of the curved section at $Y/H = 0.25$, the levels of cross-stream velocities are still high, though they are somewhat lower than those at $\theta = 60°$, showing that the decay of secondary motion outside the curved section has started. Both turbulence models produce fairly good results. It is seen that the most serious discrepancies between predictions and measurements occur along the concave surface ($Y_w/H = 0.3$). There, the cross-stream velocities are over-predicted close the symmetry plane, while they are under-predicted in a region halfway between the symmetry plane and the side wall.

In Figure 9, the predicted and measured pressure coefficients along three parallel lines within the symmetry plane ($Z/Z_{1/2} = 0$) of the duct are presented as $C_p(\theta)$. The large cross-stream pressure gradient at the inlet plane ($\theta = 0°$) confirms the influence of the bend on the upstream flow as also noted earlier in Figures 5 and 8. It can be seen that initially an adverse pressure gradient develops close to the concave surface and a favourable gradient near the convex surface, causing the observed deceleration and acceleration of the fluid near the respective surfaces in Figure 5. It is clear that these trends are reversed after around $\theta = 60°$, where the largest pressure gradient and consequently the strongest secondary motion occurs. Comparisons indicate that both turbulence models are able to reproduce the levels as well as the distributions of the measured pressure coefficients within the curved section of the curved duct with a square cross-section.

5.2. Curved duct of rectangular cross-section

Having discussed flow predictions of the curved duct with a square cross-section, attention is now directed to the performance of turbulence models in predicting flow characteristics through the curved duct with rectangular cross-section. For this test case, the predicted velocity vectors, obtained with the non-linear k–ε model, at the vertical mid-plane of the duct are shown in Figure 10. The main flow features are very similar to those observed in Figure 5 for the square curved duct. A major difference, however, between the predicted flow field in the rectangular case and that of the previous one, is that the flow in the symmetry plane of the duct is now more uniform both within and outside the curved section. This feature can

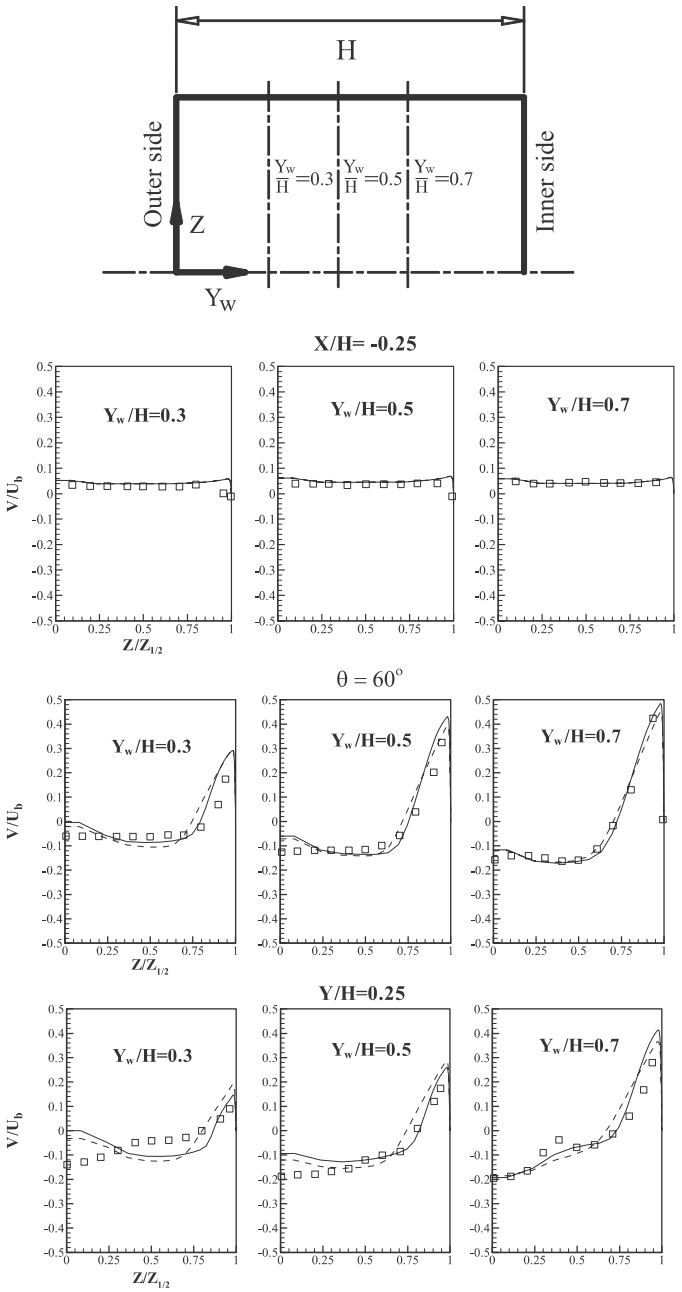

Figure 8. Comparisons between predicted and measured cross-wise velocity component for flow through a 90° bend of square cross-section. Legend as in Figure 7.

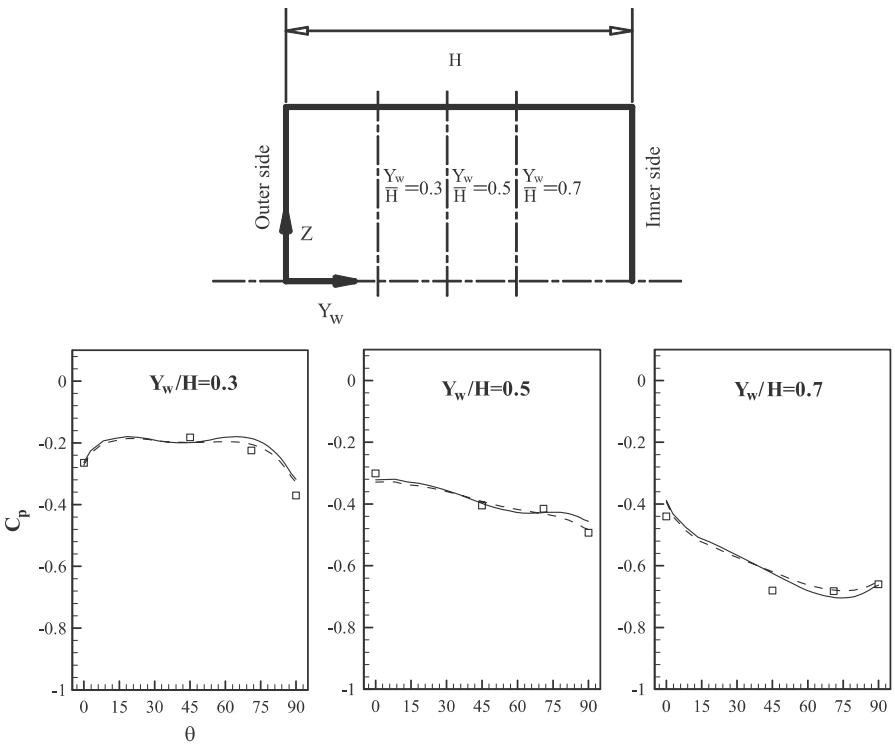

Figure 9. Local pressure coefficient comparisons for flow through a 90° bend of square cross-section. Legend as in Figure 7.

be explained by the predicted cross-duct velocity vectors and stream-wise velocity contours shown in Figure 11. As can be seen, the secondary motion close to the symmetry plane of the duct is now weaker, producing more uniform stream-wise velocity contours. Note that both turbulence models produce very similar secondary motions and stream-wise velocity contours. The only notable differences emerge near the corner regions after the bend exit, where the non-linear model returns a smaller corner vortex. This feature is consistent with comparisons shown in Figure 12. As can be seen at all locations both turbulence models produce practically identical stream-wise velocity profiles, which are also in close agreement with the experimental measurements. At the plane half a diameter before the bend, the effects of the bend on the flow are fairly minor. Half-way through the bend, the faster fluid is still displaced towards the inner side, suggesting that the effects of the entry pressure gradients still persist, while after the bend, due mainly to the exit pressure gradients, the faster fluid is displaced to the outer side. The most noticeable, all be it still minor, discrepancy between predictions and measurements occurs downstream of the curved section at $Y/H = 0.5$, close to the side wall ($Z/H = 2.5$), where the secondary motion is strongest.

In Figure 13, the predicted turbulent kinetic energy profiles are compared with the corresponding data of Kim and Patel [8]. At $X/H = -0.5$, upstream of the tangent, the results obtained with both models are much alike and are also in reasonable agreement with the data everywhere, except at the walls, where the measured data are under-predicted.

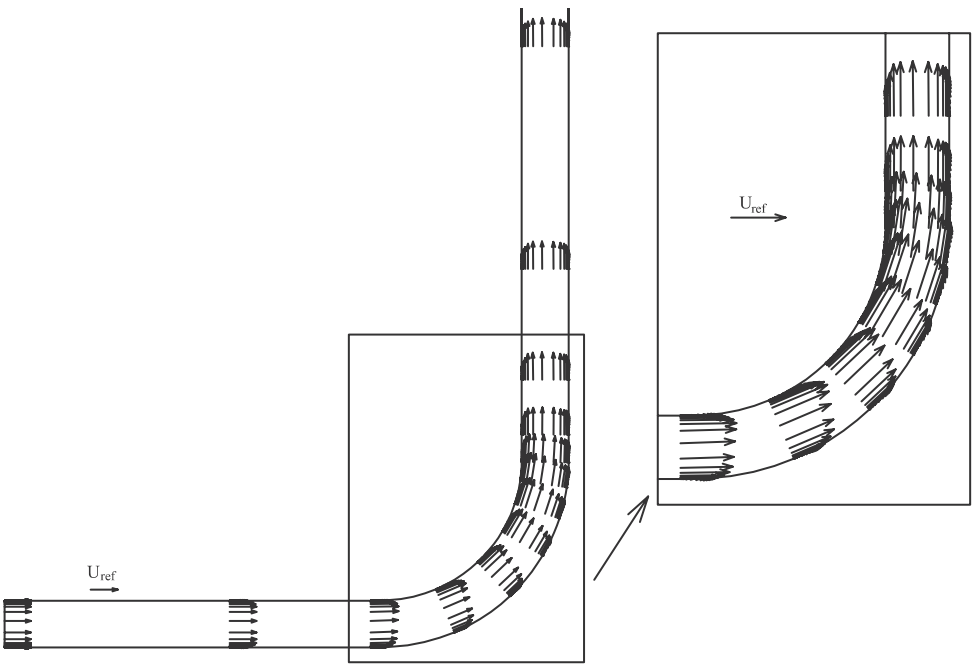

Figure 10. The predicted flow field in middle plane of the 90° bend of rectangular cross-section using the non-linear k–ε model.

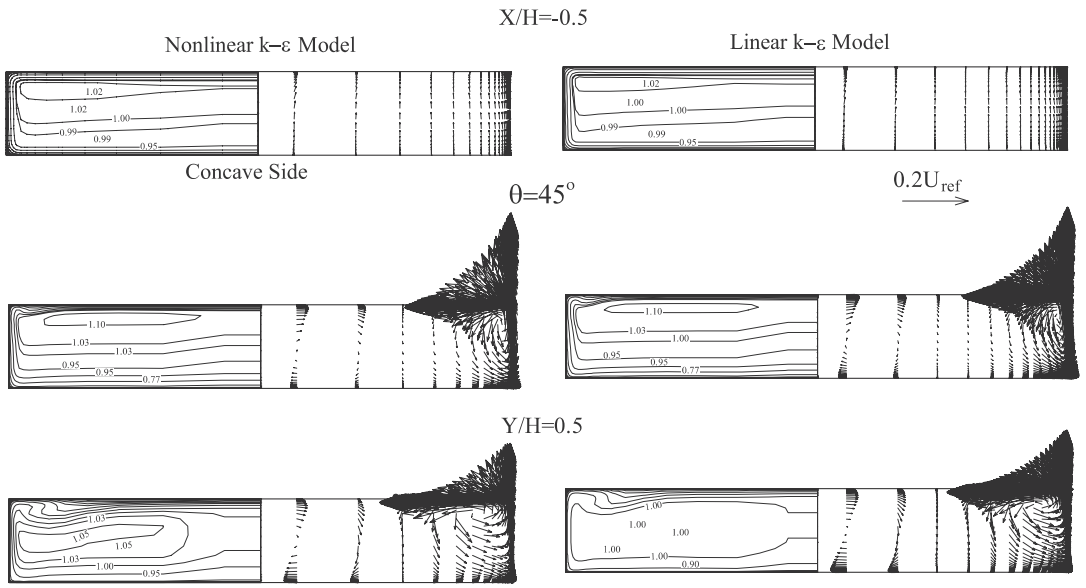

Figure 11. Predicted stream-wise velocity contours and secondary flow vectors for the 90° bend of rectangular cross-section, using the linear and non-linear k–ε models.

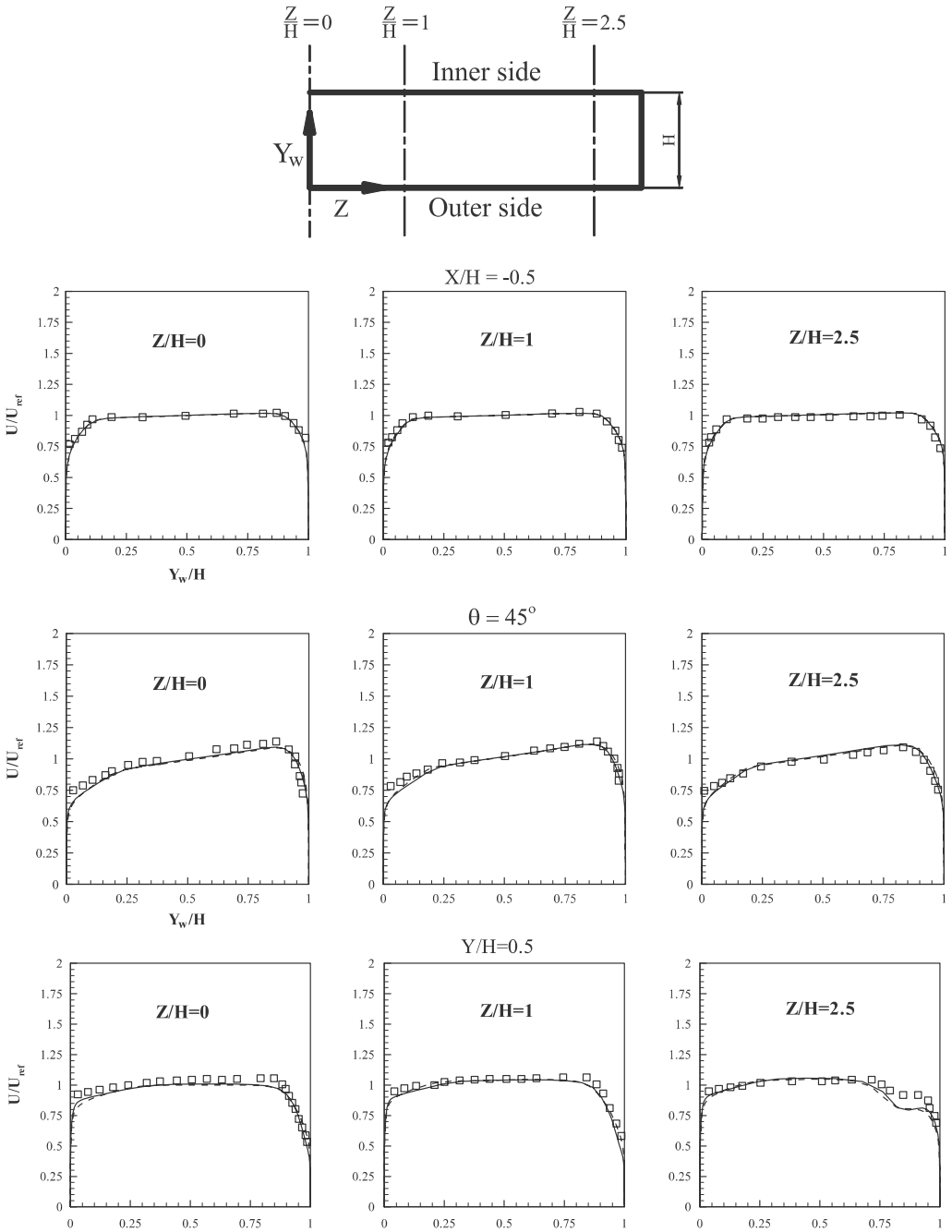

Figure 12. Comparisons between predicted and measured stream-wise velocity component for flow through a 90° bend of rectangular cross-section. Open squares: data [8]; dashed curve: linear k–ε model; solid curve: non-linear k–ε model.

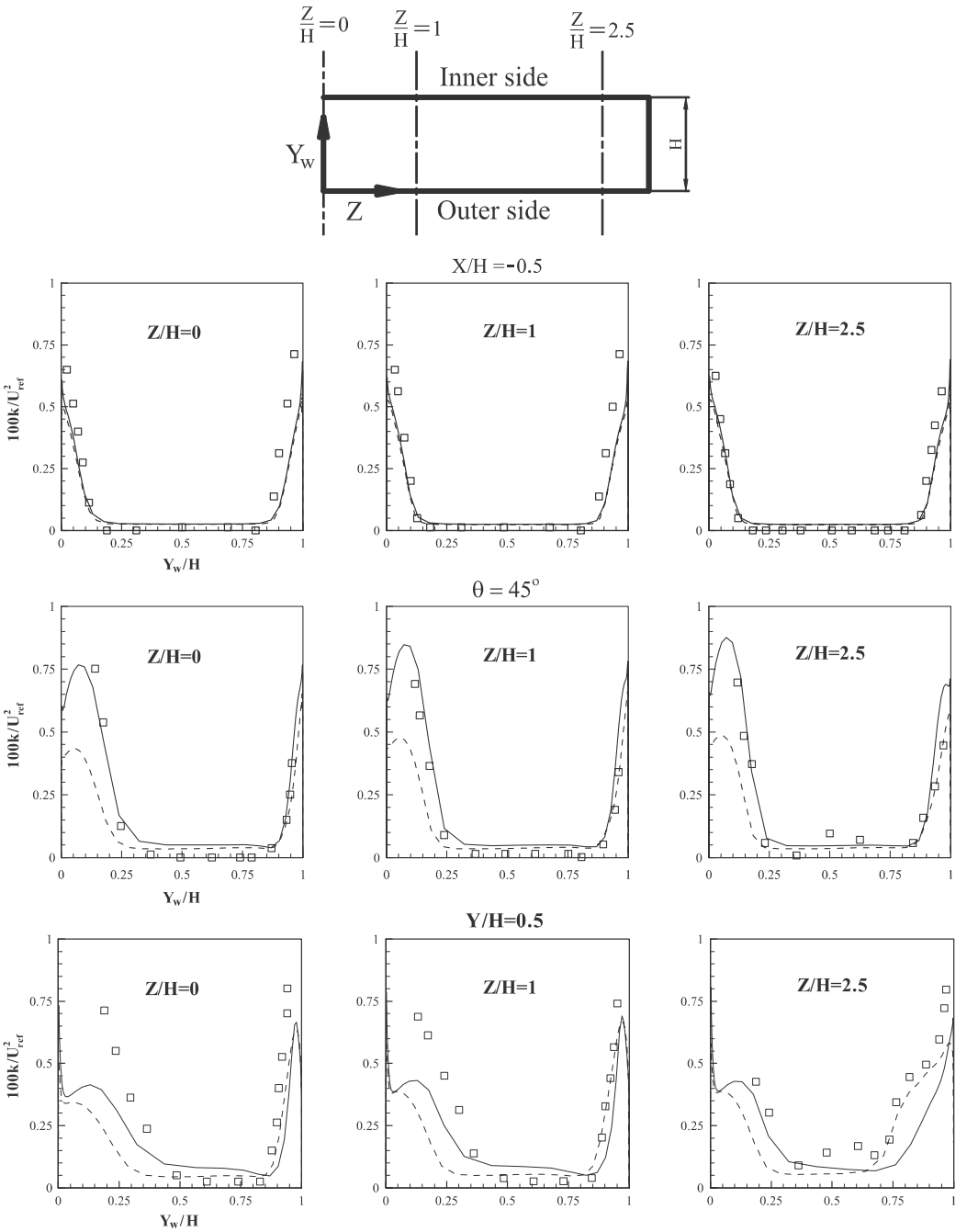

Figure 13. Comparisons between predicted and measured turbulent kinetic energy for flow through 90° bend of rectangular cross-section. Legend as in Figure 12.

Within the curved section at $\theta = 45°$, it is seen that the measured turbulence energy profiles are no longer symmetric. Along the outer wall the peak k levels are higher and also the layer of high k levels is thicker than along the inner wall. This behaviour is caused by the fact that the boundary layer over a concave surface is unstable and hence more turbulent, while over a convex surface it is stable. The linear k–ε model under-predicts the peak turbulence energy and also returns a more symmetric distribution. The non-linear model, on the other hand, reproduces the measured behaviour at all span-wise locations. This is due to the fact that direct effects of streamline curvature on turbulence cannot be reproduced with models that return isotropic turbulence, such as the EVM model. Downstream of the curved section at $Y/H = 0.5$, the variations of the measured turbulent kinetic energy profiles are also better reproduced by the non-linear k–ε model, though some discrepancies between predictions and experimental data are now present.

Considering the comparisons for turbulent shear stress profiles in Figure 14, at the first station upstream of the bend (i.e. $X/H = -0.5$) both turbulence models reproduce the shape and level of the measured profiles. Only very close to the walls the peak values of $\overline{uv}$ are under-predicted by the models. At $\theta = 45°$, as was also the case with the k comparisons of Figure 13, the non-linear k–ε model clearly performs much better than the linear model. As can be seen, the turbulent shear stress, like the turbulent kinetic energy, reaches higher peaks next to the outer surface of the duct. While the linear k–ε model again fails to reproduce this feature, the non-linear model successfully predicts the peak shear stresses. After the curved section at $Y/H = 0.5$, it is seen that the non-linear k–ε model generally is more effective in reproducing the experimental data. Note, however, that at the same location close to the side wall at $Z/H = 2.5$, the results of the linear k–ε model in a region adjacent to the inner surface of the duct are much closer to the measured data which is also consistent with the predicted turbulent kinetic energy in this location, shown in Figure 13. The experimental study of Taylor *et al.* [7] for the 90° bend of square cross-section did not provide measurement of the turbulence field. Hence, it is uncertain whether use of the non-linear k–ε model would have resulted in similar improvement in the prediction of the turbulence field for 90° bends of square cross-section.

Figure 15 demonstrates comparisons between friction coefficient profiles returned by the turbulence models and experimental data along three different stations on the concave surface. At the first station (i.e. $X/H = -0.5$) the predictions of both models are close to that data, but at the second and third stations the non-linear model predictions are clearly superior. This is not surprising because, as shown in Figures 13 and 14, the non-linear k–ε model also reproduces the turbulence field along the concave surface of the duct more reliably.

Concerning the pressure coefficient predictions in Figure 16, the data show that there is no cross-duct pressure variation before the bend, the centrifugal forces set up a strong cross-duct pressure gradient within the bend, which immediately disappears after the bend exit. Both the linear and non-linear k–ε models are able to reproduce the overall variation of the pressure coefficient within the curved section as well as the straight sections of the duct. A close examination of this figure shows that, crucially, the overall pressure drop due to the presence of the bend is more accurately predicted by the non-linear k–ε.

Finally, it should be noted that according to the experimental works the maximum experimental error in the measurements was around 5%, which is not expected to have a serious impact on any of the conclusions reached.

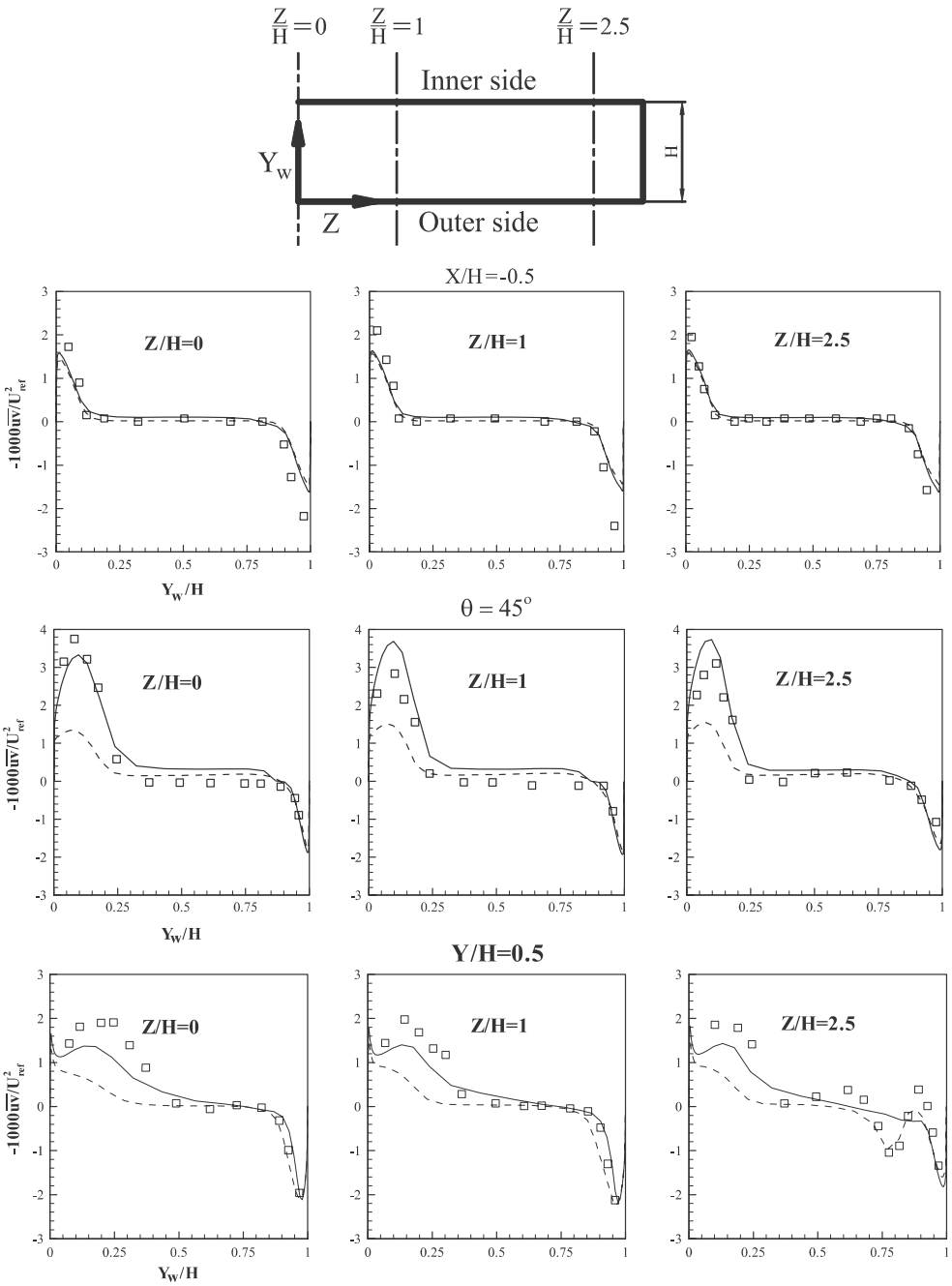

Figure 14. Comparisons between predicted and measured turbulent shear stress for flow through 90° bend of rectangular cross-section. Legend as in Figure 12.

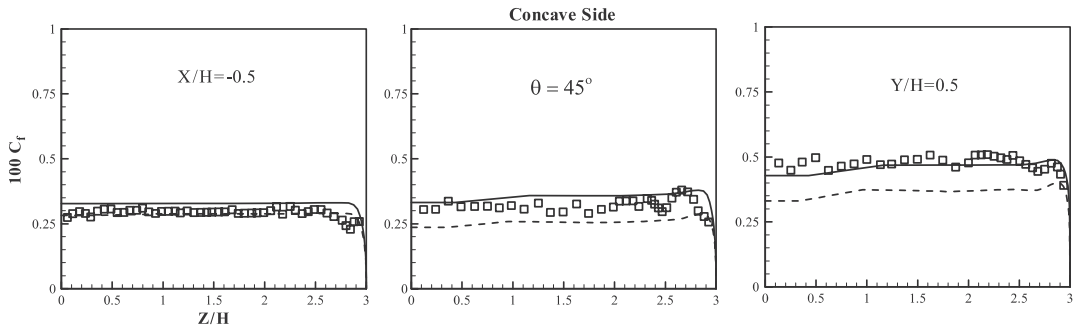

Figure 15. Local friction coefficient comparisons for flow through a 90° bend of rectangular cross-section. Legend as in Figure 12.

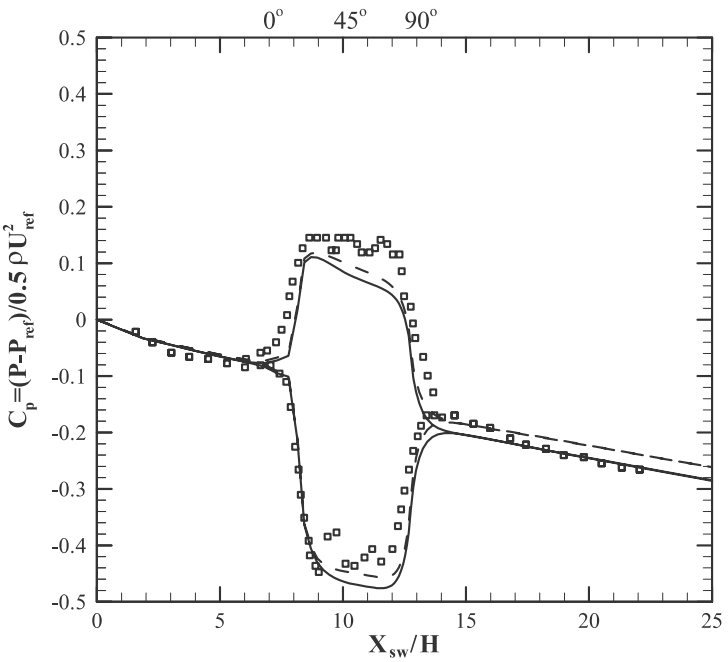

Figure 16. Pressure coefficient comparisons for flow through a 90° bend of rectangular cross-section. Legend as in Figure 12.

6. CONCLUSIONS

This study has considered the application of low-Re linear and non-linear eddy-viscosity models to the numerical prediction of the velocity and pressure fields in flow through two 90°-curved ducts, one of a square cross-section and one of a rectangular cross-section. The

computations have shown how the curvature of a 90° bend influences the flow field characteristics of developing turbulent flow. It was shown that for the bend of square cross-section the curvature induces a strong secondary motion, while for the rectangular cross-section the secondary motion is confined to the corner regions. The curvature also influences the flow development along the straight upstream section of the duct by inducing a weak cross-duct motion near the entrance of the curved section. Curvature causes the pressure gradient to change sign along the convex and concave walls of the curved section, which results in local redistribution of the stream-wise velocity profile along the curved section. The effects of curvature are also present downstream of the curved section, though slowly diminishing with the development of the main stream. In the case of bend of square cross-section an extra pair of vortices appears along the convex surface near the bend exit which results in strong span-wise gradient of the stream-wise velocity in the duct core. These features are not present in the bend of rectangular cross-section. Comparisons of the numerical predictions with the measured data for the mean velocities and pressure variation indicate that in the bend of square cross-section both turbulence models can produce reasonable predictions. For the bend of rectangular cross-section where a wider range of data is available, while both models produce satisfactory predictions of the mean flow field, the non-linear k–ε model returns superior predictions of the turbulence field and also of the pressure and friction coefficients. The main, though it has to be emphasized still minor, predictive weakness of the non-linear k–ε is in the prediction of the flow recovery after the bend exit. To address this weakness, would probably require the use of full second-moment closures that account for transport effects on the turbulent stresses.

NOMENCLATURE

C_p	pressure coefficient $\equiv [(P - P_{\text{ref}})/0.5\rho U_{\text{b}}^2]$
D_{h}	hydraulic diameter of duct
H	duct height
k	turbulent kinetic energy
P	fluid pressure
P_{ref}	reference value of pressure
P_{k}	generation rate of turbulent kinetic energy
Re	Reynolds number $\equiv [U_{\text{b}}H/v]$
R_{c}	mean radius of curvature
U	mean velocity in stream-wise direction
u	velocity fluctuation in stream-wise direction
U_{b}	bulk velocity
U_{c}	centreline velocity
U_i	mean velocity vector in tensor notation $\equiv [U, V, W]$
u_i	fluctuating velocity vector in tensor notation $\equiv [u, v, w]$
$\overline{u_i u_j}$	Reynolds stress tensor
V	mean velocity in cross-stream direction
v	velocity fluctuation in cross-stream direction
W	mean velocity in span-wise direction
w	velocity fluctuation in span-wise direction

X, Y, Z	Cartesian coordinates
x_i	Cartesian coordinates $\equiv [X, Y, Z]$
Y_w	distance from the concave wall
$Z_{1/2}$	duct half-width $\equiv [H/2]$
δ_{ij}	Kronecker delta
ε	dissipation rate of turbulent kinetic energy
$\tilde{\varepsilon}$	isotropic dissipation rate
θ	stream-wise coordinate direction
μ	fluid dynamic viscosity
ν	fluid kinematic viscosity
ρ	fluid density

REFERENCES

1. Iacovides H, Li H-Y. Near-wall turbulence modelling of developing flow through curved ducts and channels. *Proceedings of the IAHR, 5th International Symposium on Refined Flow Modelling and Turbulence Measurements*, Paris, 1993.
2. Choi Y-D, Iacovides H, Launder BE. Numerical computation of turbulent flow in a square-sectioned 180° bend. *Journal of Fluids Engineering* (ASME) 1989; **111**:59–68.
3. Enayet MM, Gibson MM, Taylor AMKP, Yianneskis M. Laser-doppler measurements of laminar and turbulent flow in a pipe bend. *International Journal of Heat and Fluid Flow* 1982; **3**:213–219.
4. Anwer M, So RMC, Lai YC. Perturbation by and recovery from bend curvature of a fully-developed turbulent flow. *Physics of Fluids* 1989; **A1**:1387–1397.
5. Sudo K, Sumida M, Hibara H. Experimental investigation on turbulent flow through a circular-sectioned 90° bend. *Experimental Fluids* 1998; **25**:42–49.
6. Humphrey JAC, Whitelaw JH. Measurements in curved flows. *Proceedings of the SQUID Conference Internal Flows*, Airlie House, 1976.
7. Taylor AMKP, Whitelaw JH, Yianneskis M. Curved ducts with strong secondary motion: velocity measurements of developing laminar and turbulent flow. *Journal of Fluids Engineering* (ASME) 1982; **104**:350–359.
8. Kim WJ, Patel VC. Origin and decay of longitudinal vortices in developing flow in a curved rectangular duct. *Journal of Fluids Engineering* 1994; **116**:45–52.
9. Sudo K, Sumida M, Hibara H. Experimental investigation on turbulent flow in a square-sectioned 90-degree bend. *Experiments in Fluids* 1991; **30**:246–252.
10. Mokhtarzadeh-Dehghan MR, Yuan YM. Measurements of turbulent quantities and bursting period in developing turbulent boundary layers on the concave and convex wall of a 90° square bend. *Experimental Thermal and Fluid Science* 2003; **27**:59–75.
11. Kreskovsky JP, Briley WR, McDonald H. Prediction of laminar and turbulent primary and secondary flows in strongly curved ducts. *NASA Report*, *No. CR.3388*, 1981.
12. Iacovides H, Launder BE, Loizou PA. Numerical computation of turbulent flow through a square-sectioned 90° bend. *International Journal of Heat and Fluid Flow* 1987; **8**(4):320–325.
13. Craft TJ, Iacovides H, Yoon JH. Progress in the use of non-linear two-equation models in the computation of convective heat transfer in impinging and separated flows. *Turbulence Flow and Combustion* 1999; **63**:59–80.
14. Raisee M, Noursadeghi A, Iacovides H. Application of a non-linear k–ε model in prediction of convective heat transfer through ribbed passages. *International Journal of Numerical Methods for Heat and Fluid Flow* 2004; **14**(3):285–304.
15. Munson BR, Young DF, Okiishi. *Fundamentals of Fluid Mechanics* (2nd edn). Wiley: New York, 1994.
16. Launder BE, Sharma BI. Application of the energy dissipation model of turbulence to the calculation of flow near a spinning disc. *Letters in Heat and Mass Transfer* 1974; **1**:131–138.
17. Iacovides H, Raisee M. Recent progress in the computation of flow and heat transfer in internal cooling passages of gas turbine blades. *International Journal of Heat and Fluid Flow* 1999; **20**:320–328.
18. Jones WP, Launder BE. The prediction of laminarization with a two-equation model of turbulence. *International Journal of Heat and Mass Transfer* 1972; **15**:301–314.
19. Gatski TB, Speziale CG. On explicit algebraic stress models for complex turbulent flows. *Journal of Fluid Mechanics* 1993; **254**:59–78.
20. Speziale CG. On non-linear k–l and k–ε models of turbulence. *Journal of Fluid Mechanics* 1987; **178**:459–475.
21. Shih TH, Zhu J, Lumley JL. A realizable Reynolds stress algebraic equation model. *NASA Technical Memorandum*, *105993*, 1993.

22. Suga K. Development and application of a non-linear eddy-viscosity model sensitized to stress and strain invariants. *Ph.D. Thesis*, Faculty of Engineering, University of Manchester, 1995.
23. Craft TJ, Launder BE, Suga K. Extending the applicability of eddy-viscosity models through the use of deformation invariants and non-linear elements. *Proceedings of the 5th International Symposium Refined Flow Modeling and Turbulence Measurements*, Paris, 1993; 125–132.
24. Lien F-S, Leschziner MA. A general non-orthogonal finite-volume algorithm for turbulent flow at all speeds incorporating second-moment turbulence closure, part 1: numerical implementation, and part 2: application. *Computer Methods in Applied Mechanics and Engineering* 1994; **114**:123–167.
25. Iacovides H. The computation of turbulent flow through stationary and rotating U-bends with rib-roughened surfaces. *International Journal for Numerical Methods in Fluids* 1999; **29**:865–876.
26. Rhie CM, Chow WL. Numerical study of the turbulent flow past an airfoil with trailing edge separation. *AIAA Journal* 1983; **21**:1525–1532.
27. Chen WL, Lien FS, Leschziner MA. Computational prediction of flow around highly-loaded compressor-cascade blades with non-linear eddy-viscosity models. *International Journal of Heat and Fluid Flow* 1998; **19**:307–319.
28. Iacovides H, Raisee M. Recent progress in the computation of flow and heat transfer in internal cooling passages of turbine blade. *International Journal of Heat and Fluid Flow* 1999; **20**:320–328.
29. Nikas K-PS, Iacovides H. The computation of flow and heat transfer through square-ended U-bends, using low-Reynolds-number models. *International Journal of Numerical Methods for Heat and Fluid Flow* 2004; **14**(3):305–324.

